ACS APPLIED MATERIALS & INTERFACES



Biological and Medical Applications of Materials and Interfaces

# Glioblastoma Therapy Using Codelivery of Cisplatin and Glutathione Peroxidase Targeting siRNA from Iron Oxide Nanoparticles

Yulin Zhang, Xiao Fu, Junsheng Jia, Tobias Wikerholmen, Kaiyan Xi, Yang Kong, Junpeng Wang, Haijun Chen, Yuan Ma, Zhiwei Li, Chuanwei Wang, Qichao Qi, Frits Thorsen, Jian Wang, Jiwei Cui, Xingang Li, and Shilei Ni

*ACS Appl. Mater. Interfaces*, **Just Accepted Manuscript** • DOI: 10.1021/acsami.0c12042 • Publication Date (Web): 04 Sep 2020



## Just Accepted



is published by the American Chemical Society. 1155 Sixteenth Street N.W., Washington, DC 20036

| | |
|---|---|
| | University, Shandong<br>Ni, Shilei; Shandong University Qilu Hospital, Department of Neurosurgery |
| | |

# Glioblastoma Therapy Using Codelivery of Cisplatin and Glutathione Peroxidase Targeting siRNA from Iron Oxide Nanoparticles

*Yulin Zhang[1], Xiao Fu[2], Junsheng Jia[3], Tobias Wikerholmen[4], Kaiyan Xi[1], Yang Kong[1], Junpeng Wang[1], Haijun Chen[1], Yuan Ma[1], Zhiwei Li[1], Chuanwei Wang[1], Qichao Qi[1], Frits Thorsen[1,4], Jian Wang[1,4] Jiwei Cui[2], Xingang Li[1], and Shilei Ni[1]**

[1]Department of Neurosurgery, Qilu Hospital and Institute of Brain and Brain-Inspired Science, Cheeloo College of Medicine, Shandong University, 107 Wenhua Xi Road, Jinan, Shandong 250012, P.R. China

[2]Key Laboratory of Colloid and Interface Chemistry of the Ministry of Education, School of Chemistry and Chemical Engineering, Shandong University, 27 Shanda South Road, Jinan, Shandong 250100, P.R. China

[3]Department of Neurosurgery, Chiping District People's Hospital, 99 Wenhua Road, Chiping, Shandong, 252100, P.R. China

[4]Department of Biomedicine, University of Bergen, Jonas Lies vei 91, 5009 Bergen, Norway

KEYWORDS: glioblastoma, ferroptosis, nanomedicine, combination chemotherapy, iron oxide nanoparticle

ABSTRACT

Glioblastoma (GBM) is the most common and lethal type of malignant brain tumor in adults. Currently, interventions are lacking, the median overall survival of patients with GBM is less than 15 months, and the postoperative recurrence rate is greater than 60%. We proposed an innovative local chemotherapy involving the construction of gene therapy-based iron oxide nanoparticles (IONPs) as a treatment for patients with glioblastoma after surgery that targeted ferroptosis and apoptosis to address these problems. The porous structure of IONPs with attached carboxyl groups was modified for the codelivery of an siRNA targeting glutathione peroxidase 4 (si-GPX4) and cisplatin (Pt) with high drug loading efficiencies. The synthesized folate (FA)/Pt-si-GPX4@IONPs exerted substantial effects on glioblastoma in U87MG and P3#GBM cells, but limited effects on normal human astrocytes (NHAs). During intracellular degradation, IONPs significantly increased iron ($Fe^{2+}$ and $Fe^{3+}$) levels, while Pt destroyed nuclear DNA and mitochondrial DNA, leading to apoptosis. Furthermore, IONPs increased $H_2O_2$ levels by activating NADPH oxidase (NOX). The Fenton reaction

between $Fe^{2+}$, $Fe^{3+}$ and intracellular $H_2O_2$ generated potent reactive oxygen species (ROS) to initiate ferroptosis, while the coreleased si-GPX4 inhibited GPX4 expression and synergistically improved the therapeutic efficacy through a mechanism related to ferroptosis. As a result, superior therapeutic effects with low systemic toxicity were achieved both *in vitro* and *in vivo*, indicating that our nanoformulations might represent safe and efficient ferroptosis and apoptosis inducers for use in combinatorial glioblastoma therapy.

## INTRODUCTION

Glioma is one of the most lethal and treatment-resistant cancers. Gliomas are classified into 4 grades (WHO I, II, III, and IV) based on the level of malignancy, with type IV glioma or glioblastoma (GBM) being the most lethal form of glioma.[1,2] Despite decades of research, surgical resection is still regarded as the fundamental treatment for GBM and is the most common intervention offered to patients with GBM.[3] Combination therapy encompassing surgical resection, chemotherapy, and radiation offers a minimal increase in the clinical benefit, with the median survival of patients reported to be less than 15 months.[3,4]

Based on accumulating evidence, GBM cells invade and infiltrate the surrounding normal brain tissue, increasing the difficulty of the current curative resection approach.[5,6] The therapeutic effect of chemotherapy drugs alone has proven disappointing due to several factors, including insufficient delivery across the blood-brain barrier (BBB), side effects involving somatic functions, and increased drug resistance. Therefore, researchers have expended a great effort to develop novel therapeutic approaches designed to combat GBM.[7,8] Researchers are constantly

exploring combinations of different chemotherapies targeting different intracellular pathways that are potentially associated with carcinogenesis.[9] According to several clinical studies, combination chemotherapy may prolong the survival time and reduce the recurrence rate. Furthermore, drug specificity and chemoresistance have been ameliorated by these combination treatments.[10-12] Thus, our research focuses on improving combination therapies, not by combining classical chemotherapeutics but instead by combining treatments targeting two pathways, specifically, the induction of apoptosis and a newly discovered form of controlled cell death, ferroptosis. This combination might exhibit a maximal antitumor effect.

Ferroptosis was recently identified as an innovative target for the treatment of malignant cancers. Ferroptosis is a type of iron-dependent programmed cell death that is distinct from other forms of cell death, such as necroptosis, apoptosis, pyroptosis, autophagy, and paraptosis.[13-15] Excess iron reacts with hydrogen peroxide ($H_2O_2$) intracellularly to generate hydroxyl radicals and singlet oxygen through a process referred to as the Fenton reaction.[16] A high level of hydroxyl radicals eventually leads to lipid peroxidation, which is cytotoxic to the cell.[17,18] Since ferroptosis is significantly

different from apoptosis in terms of the mechanism and phenotype, combination treatment targeting these two processes may be a strategy for treating GBM. However, this type of promising GBM treatment strategy has rarely been studied to date.

Our approach consists of combining a common chemotherapeutic drug with iron particles to effectively treat GBM cells.[19] Iron oxide nanoparticles (IONPs) have been identified as the most efficient and accessible carriers for the delivery of iron ($Fe^{2+}$/$Fe^{3+}$) into cells. These particles have been developed to increase the drug concentration at the tumor site through both active and passive transport.[20,21] Nanoparticles enable the loading of traditional chemotherapeutics and thus form the basis of our proposed combination treatment. In this system, iron particles initiate a Fenton reaction as a starting point for ferroptosis, while the chemotherapeutic drug induces apoptosis.[22] A high intracellular concentration of ROS must be present to induce the maximum degree of lipid peroxidation. This process requires the rapid release of large amounts of iron, particularly $Fe^{2+}$, from the nanoparticles as a sufficient substrate for the Fenton reaction.[23] Through these microsecond-level processes, a large amount of hydroxyl radicals are energetically generated, causing lipid peroxidation and leading to tumor cell

death.[24] Among the plethora of synthetic carriers, IONPs represent a promising material for drug delivery and nanoparticle-based therapy for several reasons. First, IONPs are biocompatible and biodegradable drug carriers that have been clinically tested and approved by the FDA.[25] Second, IONPs significantly increase the intracellular iron content and interfere with normal iron metabolism in cells.[26,27] Last but not least, IONPs display superparamagnetic properties, allowing them to be directionally conveyed by an external magnetic field. This property is important for Magnetic Resonance Imaging (MRI), photodynamic therapy, and hyperthermia.[28,29] Therefore, IONPs appear to be promising candidates for further research, particularly regarding their potential use in cancer treatment.

Based on these findings, we designed an IONP-based system that efficiently delivers iron, cisplatin (Pt), and a glutathione peroxidase 4 (GPX4) small interfering RNA (si-GPX4) for the highly efficient synergistic induction of ferroptosis/apoptosis in GBM cells (Scheme 1). We applied a porous IONP platform containing carboxyl groups that do not require further surface modification for iron accommodation, with iron serving as a trigger for the Fenton reaction. Functional si-GPX4 was loaded into our nanodrug to

maximize the antitumor effect of ferroptosis. These si-GPX4 particles retain the gene knockdown ability of the antisense strand, and amino groups and 5-carboxyfluorescein (FAM, green fluorescence) were added to the sense strand. Subsequently, the carboxyl groups of the IONPs and the amino groups of si-GPX4 were covalently bonded following catalysis by 1-ethyl-3-(3-(dimethyl amino) propyl) carbodiimide (EDC) and n-hydroxy succinimide (NHS). Pt was loaded onto the si-GPX4@IONPs through electrostatic adsorption. Pt was chosen due to its ability to induce apoptosis in target cells and its role in increasing intracellular $H_2O_2$ levels. Finally, 1,2-distearoyl-sn-glycero-3-phosphoethanolamine-N-[folate(polyethylene glycol)-2000] (DSPE-PEG2K-FA) was incorporated into Lipofectamine to ultimately yield the nanodrug, FA/Pt-si-GPX4@IONPs. The Lipofectamine reagent is extensively accepted as the “gold standard” for the delivery of exogenous DNA or RNA into cells. According to previous studies, liposomes protect the integrity of exogenous DNA or RNA and therefore facilitate the retention of desired functions when applied *in vitro* or *in vivo*.[30] The presence of flexible PEG2K enhances the ability of tumor cells to accept nanodrugs and reduces the aggregation of nanoparticles and protein adsorption,[31] thereby improving

the efficiency of nanodrug targeting and internalization. We studied the effects of our drug on three appropriate cells lines: a common human glioblastoma cell line (U87MG), a primary glioblastoma cell line (P3#GBM), and normal human astrocytes (NHAs). *In vitro*, the synthesized FA/Pt-si-GPX4@IONPs nanoparticles increased apoptosis and ferroptosis rates in U87MG and P3#GBM cells. FA/Pt-si-GPX4@IONPs nanoparticles displayed outstanding therapeutic effects *in vivo*. Based on our results, the synthesized FA/Pt-si-GPX4@IONPs show promise and potential as a treatment for glioblastoma, and this nanodrug is expected to become a candidate for local chemotherapy in patients with glioma after surgery. The effectiveness of this nanodrug system shows promise as a prototype for the design of practical combination strategies for glioma treatment.

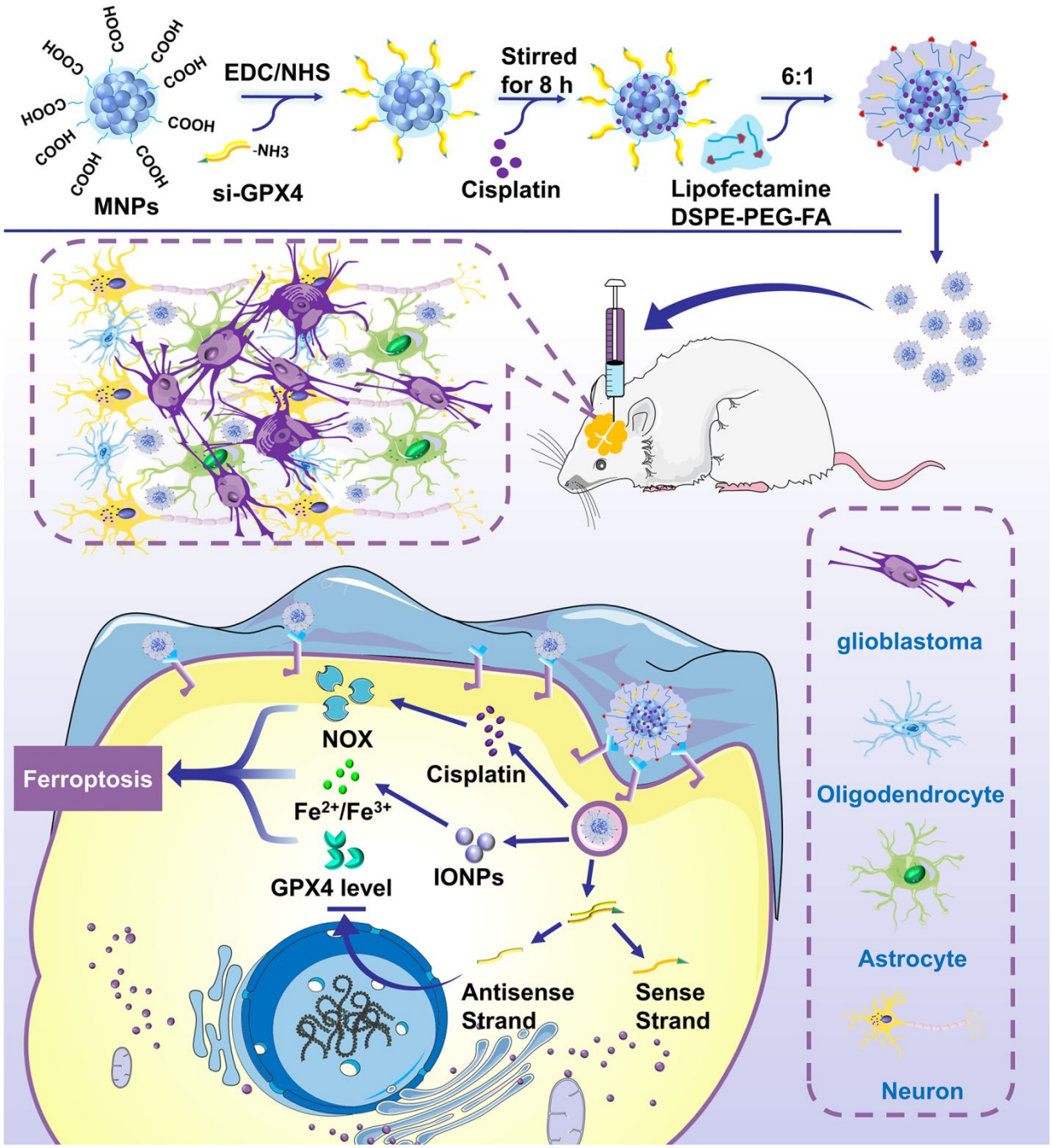


**Scheme 1.** Design and synthesis of our nanoparticles and illustration of the mechanism of combination therapy of orthotopic glioblastoma with FA/Pt+si-GPX4@IONPs through the induction of ferroptosis and apoptosis.

## EXPERIMENTAL SECTION

**Materials.** IONPs were purchased from Beijing Zhongkeleiming Daojin Technology (Beijing, China). EDC, NHS, and a Live/Dead Viability/Cytotoxicity Kit were purchased from Sigma-Aldrich (St. Louis, MO, USA). DSPE-PEG2K-FA and 1,2-distearoyl-sn-glycero-3-phosphoethanolamine-N-[amino(polyethylene glycol)-2000]-N-(cyanine 7) (DSPE PEG2K-Cy7) were obtained from Xi'an Ruixi Biological Technology (Xi'an, China). Lipofectamine 2000 was obtained from Thermo Fisher Scientific (Waltham, MA, USA). An anti-FOLR2 antibody (ab56067) and an iron colorimetric assay kit were purchased from Abcam (Cambridge, UK). A rabbit polyclonal anti-folate receptor 1 (FOLR1) antibody was obtained from Proteintech Group (Wuhan, China). Malondialdehyde (MDA), dihydroethidium (DHE), and glutathione (GSH) and glutathione disulfate (GSSG) assay kits were obtained from Beyotime Biotechnology (Nanjing, China). Cell Counting Kit-8 (CCK-8) was purchased from Dojindo Laboratories (Kumamoto, Japan).

**Preparation of FA/Pt+si-GPX4@IONPs.** FA/Pt+si-GPX4@IONPs were synthesized using a three-step strategy. First, 1 mL of porous IONPs containing carboxyl groups (10

mg/mL) were prepared in diethyl pyrocarbonate (DEPC)-treated water, pH 6, mixed with 9.6 mg of EDC and 5.8 mg of NHS and stirred at room temperature (RT) for 1 h. The si-GPX4 sequences, including si-GPX4#1 and si-GPX4#1 (sense strand of si-GPX4#1: 5'-GTGGATGAAGATCCAACCCAA-3', sense strand of si-GPX4#1: 5'-GCACATGGTTAACCTGGACAA-3'), which targeted GPX4 in the ferroptotic signaling pathway, were synthesized by Gene Pharma (Shanghai, China). For fluorescence observations, the 5' end of the sense strand was labeled with 5-carboxyfluorescein (FAM). For the purpose of loading on the IONPs, the sense strand was also modified with amino groups. The solution obtained from the first step was added to si-GPX4 at different IONPs/si-GPX4 (I/S) ratios for 30 min. The obtained si-GPX4@IONPs were analyzed using agarose gel electrophoresis to assess the binding affinity. RNase A (3 ng/mL) was applied to FA/Pt+si-GPX4@IONPs at an I/S ratio of 16 or free si-GPX4 to evaluate protective ability.

In the second step, Pt loading, 10 mg/mL si-GPX4@IONPs were mixed with 3 mg/mL Pt and stirred for 8 h. After sufficient electrostatic adsorption, the mixture was

centrifuged at 1000 rpm in an ultrafiltration centrifuge tube (molecular weight: 10 kDa) in the dark to remove free Pt.

The prepared lipid film composed of Lipofectamine 2000 and DSPE-PEG2K-FA at a molar ratio of 6:1 was hydrated with DEPC-treated water containing 1 mg/mL Pt+si-GPX4@IONPs to coat the Pt+si-GPX4@IONPs with liposomes. The mixed solution was extruded through a 200 nm polycarbonate membrane and purified on Sephadex G-100 columns. The obtained FA/Pt+si-GPX4@IONPs were condensed and stored at 4 °C until further use.

**Characterization.** Transmission electron microscopy (TEM; JEM-1400, Tokyo, Japan) and scanning electron microscopy (SEM; EVO 18, Zeiss, Germany) were used to analyze the morphologies of the obtained nanoparticles. A Zetasizer Nano-S90 analyzer (Malvern Instruments, UK) was used to measure the zeta potentials and sizes of the obtained nanoparticles at a fixed scattering angle of 173° and a temperature of 25 ± 0.1 °C. A NexION 350X ICP-MS instrument (Perkin-Elmer, Ohio, USA) was used to detect the drug loading efficiency and release curve.

For TEM observations of cells, the cells were incubated with 100 μg/mL IONPs for 6 h and then collected from the culture dishes. Briefly, cell pellets were fixed with phosphate-buffered saline (PBS) containing 2.5% glutaraldehyde and 4% paraformaldehyde for 4 h. After washing, embedding, and fixation, the samples were stained with 0.5% uranyl acetate for 1 h and dehydrated in ethanol. Then, the samples were embedded in epoxy resin and polymerized at 60 °C for 48 h. After being sliced into 60-80 nm ultrathin sections and stained with 5% aqueous uranyl acetate and 2% aqueous lead citrate, the samples were observed using TEM.

**Cell Lines and Culture.** The human glioma cell line U87MG was purchased from the Chinese Academy of Sciences Cell Bank (Shanghai, China). NHAs and primary human GBM biopsy-propagated P3#GBM tumor cells were kindly provided by Prof. Rolf Bjerkvig, the Department of Biomedicine, the University of Bergen, Norway. U87MG cells and NHAs were cultured in Dulbecco's Modified Eagle's Medium (DMEM; Thermo Fisher Scientific) supplemented with 10% fetal bovine serum (FBS; Thermo Fisher Scientific) in a humidified incubator containing 5% $CO_2$ at 37 °C. P3#GBM cells were cultured in Neurobasal Medium (Gibco, Thermo Fisher Scientific) supplemented with 2%

B27 Neuro Mix (Thermo Fisher Scientific), 20 ng/mL epidermal growth factor (EGF; Thermo Fisher Scientific), and 10 ng/mL basic fibroblast growth factor (bFGF; PeproTech; Rocky Hill, NJ, USA) in a humidified incubator containing 5% $CO_2$ at 37 °C.

**Immunohistochemistry.** The mice were sacrificed, and tissue samples were fixed with 4% paraformaldehyde in PBS, embedded in paraffin and cut into 4 μm sections. The sections were dewaxed and rehydrated and then incubated with 0.01 M citrate buffer for 20 min at 95 °C for antigen retrieval. Endogenous peroxidase activity was blocked with 3% $H_2O_2$ (ZSGB-Bio; Beijing, China), and nonspecific antigens were blocked with 10% normal goat serum (ZSGB-Bio). Then, the sections were incubated with one of the following primaries antibodies at 4 °C for 12 h: rabbit anti-GPX4 (ab125066, 1:200; Abcam) and rabbit anti-Ki67 (ab15580, 1:500; Abcam). The sections were washed with PBS three times for 5 min each and incubated with a goat anti-rabbit secondary antibody (ZSGB-Bio). The antigens were visualized by applying 3,3'-diaminobenzidine (DAB, ZSGB-Bio), and the slides were counterstained with hematoxylin (Beyotime; Shanghai, China) at 25 °C for 2 min. Negative control sections were incubated with normal goat serum instead of the primary antibody.

**Cell Viability and Proliferation Assays.** Cell viability was assessed using the CCK-8 assay according to the manufacturer's protocol. Cells were seeded in 96-well plates at a density of $2\times10^3$ cells/well and incubated at 37 °C for 24 h in a humidified incubator containing 5% $CO_2$. The CCK-8 solution (10 μL) was added to each well, and the plates were incubated for 1 h at 37 °C in the incubator. The optical absorbance of each well was read at 450 nm (OD450) using a microplate reader (Bio-Rad; Hercules, CA, USA). Proliferation was assessed using the EdU incorporation assay according to the manufacturer's protocol (Rib-bio; Guangzhou, China). Briefly, EdU was incorporated into the treated cells and detected through a catalyzed reaction with a fluorescently labeled azide. Cells in each group were examined under a fluorescence microscope, and the number of EdU-positive cells among a total of 500 cells was counted in three independent experiments.

**Iron Assay.** The $Fe^{2+}$ concentration was analyzed using an iron colorimetric assay kit (Abcam; California, USA) according to the manufacturer's instructions. Briefly, the treated cells were added to the iron assay buffer on ice and centrifuged at 16000 × g for 10 min at 4 °C to obtain the supernatant. Fifty microliters of the supernatant were

incubated with 50 μL of assay buffer in a 96-well microplate for 30 min at 25 °C. Then, the samples were incubated with 100 μL of the iron probe for 60 min at 25 °C in the dark. The absorbance (593 nm) was measured using a microplate reader (Bio-Rad). The $Fe^{2+}$ concentration was calculated with the following formula: (Sa/Sv) * D, with Sa representing the content of $Fe^{2+}$ in the sample well calculated from the standard curve (nM), Sv representing the volume of sample added into the reaction wells (μL), and D representing the sample dilution factor.

**Lipid Peroxidation Assessment.** Lipid peroxidation levels were detected using an MDA assay kit (Beyotime). According to the protocol, lysis buffer was added to the cells, the cells were homogenized on ice, the mixtures were centrifuged at 1600 × g for 10 min at 4 °C, and then the supernatant was collected. One hundred microliters of each supernatant were incubated with 100 μL of the test solution for 15 min at 100 °C and then cooled to RT. The mixtures were centrifuged at 1000 × g for 10 min to obtain supernatants, and the absorbance was read at 530 nm using a microplate reader (Bio-Rad). The MDA content was expressed as a ratio of the absorbance values of treated cells and control cells.

**Superoxide Anion Detection.** Superoxide anion levels were detected using DHE (Beyotime). The cells were cultured in 8-well μ-Slide chamber slides (Ibidi; Martinsried, Germany) for 24 h and then treated with nanoparticles for 24 h. Treated cells were washed three times with PBS and then loaded with DHE (10 mmol/L) in fresh medium at 37 °C for 30 min. Fluorescence was measured using a Leica SP8 confocal microscope (Leica Microsystems; Wetzlar, Germany). The levels of superoxide anions are presented as the ratio of the absorbance values of treated cells and control cells.

**Live/Dead Staining.** The numbers of live and dead cells were assessed using a Live/Dead Viability/Cytotoxicity Kit (Sigma-Aldrich, Missouri, USA) according to the manufacturer's protocol. Briefly, calcein-AM and ethidium homodimer-1 working solutions were prepared in PBS at the proper dilutions. The staining solutions were mixed with the medium at a ratio of 1:2 (v/v) and incubated with the cells at 37 °C for 15 min. Images of live and dead cells were captured using a Leica SP8 confocal microscope (Leica Microsystems).

**Animal Studies.** All experimental procedures were approved by the Research Ethics Committee of Shandong University and the Ethics Committee of Qilu Hospital

(Shandong, China). The Institutional Animal Care and Use Committee (IACUC) of Shandong University approved all animal procedures performed in our study. For intracranial xenograft studies, luciferase-labeled U87MG glioma cells were implanted into 4-week-old female nude mice (Foxn1$^{nu}$ mut/mut; SLAC Laboratory Animal Center; Shanghai, China). The mice were divided into five groups (ten mice per group): the saline-, Pt, Pt@IONP-, Pt+si-GPX4@IONP-, and FA/Pt+si-GPX4@IONP-treated groups. The mice were anesthetized with an intraperitoneal injection of 80 μL of ketamine HCl (25 mg/ml), xylazine (2.5 mg/ml), and 14.25% ethyl alcohol (diluted 1:3 in 0.9% NaCl). A total of 1 x $10^6$ cells were diluted in 10 μL of PBS and then injected into the right frontal lobe of each mouse (1 mm anterior and 2.5 mm lateral to bregma at a depth of 2 mm). Tumor growth was monitored with bioluminescence imaging (BLI) using *In Vivo* Imaging System (IVIS) Spectrum (Perkin-Elmer; Waltham, MA). Animals that displayed symptoms (such as a severe hunchback posture, apathy, decreased motion or activity, dragging legs, unkempt fur, or a drastic loss of body weight) were sacrificed by cervical dislocation. The mice were then perfused with physiological saline and 4% paraformaldehyde (PFA). The brains and major organs were harvested and further fixed

with 4% PFA before being embedded in paraffin. Tumor tissues were further examined using hematoxylin and eosin (H&E) and immunohistochemical (IHC) staining.

**Statistical Analysis.** Student's t-test was used to compare the mean values of paired data. ANOVA was used to analyze potential differences between multiple groups. Kaplan-Meier survival curves were compared using the log-rank test to assess differences in survival between groups. Statistical analyses were conducted using GraphPad Prism version 7.00 software (GraphPad; La Jolla, CA, USA). All experiments were repeated at least three times unless stated otherwise. The data obtained from each treatment group are presented as the means ± standard error of the mean (SE). All tests were two-sided, and p-values $< 0.05$ were considered statistically significant.

## RESULTS AND DISCUSSION

**Preparation and Characterization of FA/Pt-si-GPX4@IONPs.** Emerging evidence suggests a critical role for nonmutational drug resistance mechanisms in regulating the survival of residual glioblastoma "persister" cells.[32,33] GPX4 has been identified as a key regulator of acquired drug resistance in cancer cells, as the loss of GPX4 function results in the ferroptotic death of selective persister cells *in vitro* and prevents tumor

relapse *in vivo.*[34] Thus, approaches targeting GPX4 appear to be a viable therapeutic strategy to prevent acquired drug resistance.[35,36] At the molecular level, cysteine availability, GSH biosynthesis and proper functioning of GPX4 are critical for restraining ferroptosis. Importantly, functional inhibition or knockdown of GPX4 triggers ferroptotic cell death.[37,38] We synthesized GPX4-specific siRNAs and a negative control siRNA, transfected them into U87MG cells, P3#GBM cells and NHAs for 48 h, and tested the knockdown efficiency to confirm this finding. The qRT-PCR results showed a distinct decrease in the levels of the GPX4 mRNA in all three cell lines (Supplementary Figure 1a, $p < 0.001$, $n = 3$). Furthermore, GPX4 knockdown inhibited the proliferation of U87MG cells, P3#GBM cells and NHAs, as evidenced by the results of the CCK-8 assay (Supplementary Figure 1b, $p < 0.01$, $n = 3$).

We modified the surface of our nanoparticles with FA to create IONPs with specific biological targeting properties. We selected this targeting molecule based on the levels of FOLR1 and folate receptor beta (FOLR2) in human glioblastoma (U87MG and P3#GBM) cells and NHAs. Data were collected from a database publicly available from Gene Expression Profiling Interactive Analysis (GEPIA). An analysis of the database

revealed significantly increased levels of the FOLR1 and FOLR2 mRNAs in glioblastoma cells (Supplementary Figure 2a and b). Next, we performed western blotting to evaluate the levels of the FOLR1 and FOLR2 proteins in our selected cell lines. Compared to NHAs, the levels of the FOLR1 and FOLR2 proteins were increased in our human glioblastoma cells (Supplementary Figure 2c and d).

Commercially available porous IONPs with a diameter of 80 nm were selected as the iron nanoparticles for our experiments. The IONPs were synthesized using a novel three-step loading and coating method developed in our laboratory. Interestingly, the carboxyl group of IONPs reacted with the amino group of si-GPX4. However, as the amino group of si-GPX4 was only modified on the sense strand, the gene knockdown function of the antisense strand was retained. Pt was absorbed into the structural skeleton of the IONPs through electrostatic adsorption. The resulting nanoparticles, Pt+si-GPX4@IONPs, were coated with a mixture of DSPE-PEG2K-FA and Lipofectamine under nitrogen protection. After the nanoparticles were coated, the FA/Pt+si-GPX4@IONPs were tested in an aqueous phase (Figure 1a).

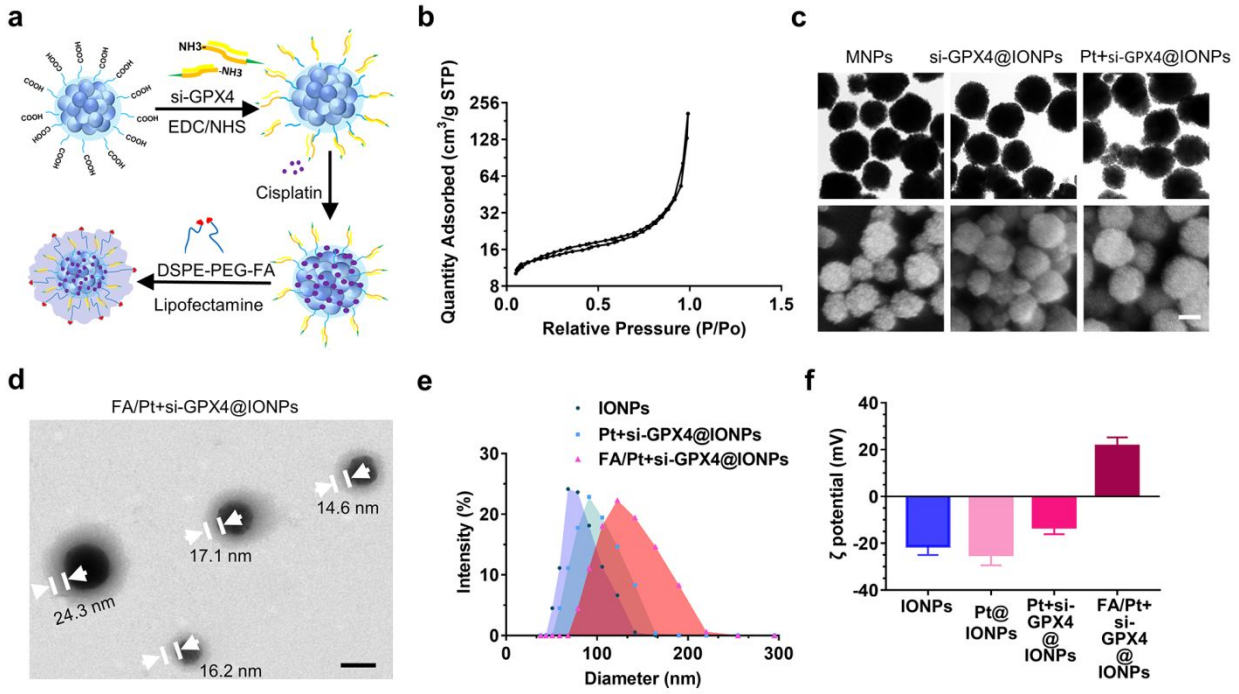


**Figure 1.** (a) Schematic illustrating the fabrication and drug loading process of IONPs. (b) Brunauer-Emmett-Teller (BET) analysis of the surface area of IONPs. (c) TEM and SEM images of IONPs, si-GPX4@IONPs, and Pt+si-GPX4@IONPs. Scale bar: 50 nm. (d) TEM image of FA/Pt+si-GPX4@IONPs; the white arrows indicate the nanolayers of the nanoparticles. Scale bar: 80 nm. (e) Size distributions of IONPs, Pt+si-GPX4@IONPs, and FA/Pt+si-GPX4@IONPs. (f) Zeta potentials of IONPs, si-GPX4@IONPs, Pt+si-GPX4@IONPs, and FA/Pt+si-GPX4@IONPs (n = 3). Data are shown as the mean ± SE for each group.

Brunauer-Emmett-Teller (BET) analysis shows that the surface area of IONPs is 46.773 $m^2$ /g, and pore size is 6.8-9.3 nm (Figure 1b). TEM images showed a rough surface of our IONPs with many observable pores (Figure 1c). After the IONPs were loaded with si-GPX4 and cisplatin, the si-GPX4@IONPs nanoparticles were covered with a thin 6.2±2.5 nm nanolayer that was observed on the outermost surface of the particles using low contrast. This nanolayer was not detectable in nude IONPs (Figure 1c and Supplementary Figure 3). SEM images showed the morphology of the si-GPX4@IONPs and Pt+si-GPX4@IONPs, revealing that the compound nanoparticles were more “glossy” than the nude IONPs (Figure 1c). Encapsulation of the Pt+si-GPX4@IONPs within liposomes was performed by hydrating a prepared lipid film composed of Lipofectamine 2000 and DSPE-PEG2K-FA at a molar ratio of 6:1 with a DEPC solution of 1 mg/mL Pt+si-GPX4@IONPs. As observed using TEM, the obtained FA/Pt+si-GPX4@IONPs exhibited a thicker nanolayer of approximately 18.6±5.3 nm that was easily distinguishable from the thinner nanolayer observed on Pt+si-GPX4@IONPs (Figure 1d). Dynamic light scattering (DLS) was performed to determine the hydrodynamic diameter of molecules; the diameters of IONPs, Pt+si-GPX4@IONPs,

and FA/Pt+si-GPX4@IONPs were 78.8 nm, 91.3 nm and 122.4 nm, respectively. Thus, the endocytosis of these synthesized nanoparticles would not be hindered due to their size (Figure 1e). Due to a large number of exposed carboxyl groups, our IONPs had a negative surface potential of -21.27±3 mV. After loading si-GPX4 and cisplatin, the zeta potentials of si-GPX4@IONPs and Pt+si-GPX4@IONPs were -24.91±3.62 mV and 13.11±2.45 mV, respectively. When coated with Lipofectamine and DSPE-PEG2K-FA, the zeta potential of our nanoparticles was 21.5±3.04 mV (Figure 1f, n = 3).

Notably, si-GPX4 was loaded onto our IONPs via interactions between carboxyl groups and amino groups. The efficiency of the interaction between IONPs and si-GPX4 was detected at I/S ratios (by weight) of 1, 2, 4, 8, 16, 32, 64, and 128. Agarose gel electrophoresis showed unbound si-GPX4 at different I/S ratios. A considerable amount of unbound si-GPX4 was observed at I/S ratios of 1, 2, 4, and 8. The amount of unbound si-GPX4 was significantly decreased at an I/S ratio of 16, while most of the si-GPX4 was bound at I/S ratios of 32, 64, and 128 (Figure 2a). The quantitative analysis of the si-GPX4 concentration also showed that more than 85% of si-GPX4 bound to IONPs when the I/S ratio was 32, and the amount of si-GPX4 loading was 2.58%

(Figure 2b, n = 3). Inefficient si-GPX4 loading was perhaps due to the amount of carboxyl groups. However, the si-GPX4 that did bind to the IONPs was still sufficient for GPX4 knockdown. The GPX4 knockdown efficiency was 90.3%, 90.6%, 83.0%, and 57.7% of the control level at I/S ratios of 16, 32, 64, and 128, respectively (Figure 2c, $p < 0.01$, n = 3). As RNase is ubiquitous in the environment and bodies of organisms, our coated nanoparticles play a crucial role in properly protecting si-GPX4 from RNase degradation. Therefore, we performed an RNase degradation assay in which free si-GPX4 and FA/Pt+si-GPX4@IONPs were exposed to RNase for different periods. The release of siRNA was observed using agarose gel electrophoresis. Half of the free si-GPX4 was degraded after a 6 h incubation period, with most of the si-GPX4 being degraded after 48 h. However, the protection provided by Lipofectamine and PEG allowed most of the si-GPX4 bound to FA/si-GPX4@IONPs to remain intact after a 72 h incubation period (Figure 2d).

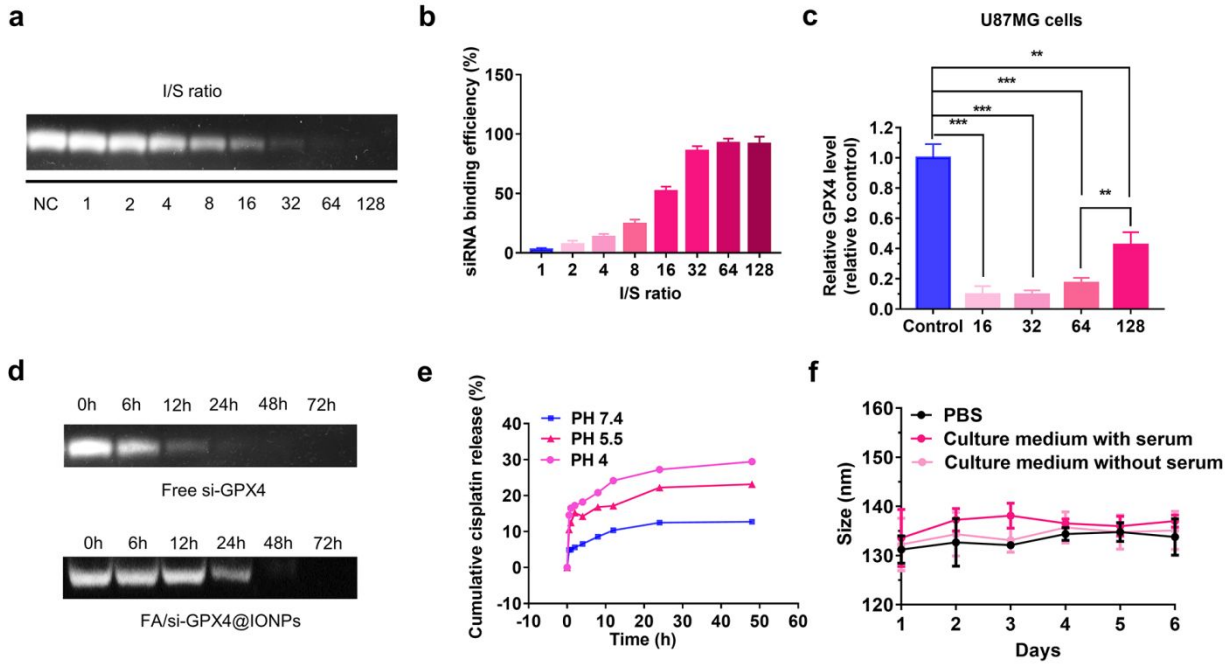


**Figure 2.** (a) Agarose gel electrophoresis of si-GPX4 bonded to IONPs at different I/S ratios. (b) si-GPX4 binding efficiency at different I/S ratios (n = 3). (c) qRT-PCR was used to detect the levels of the GPX4 mRNA in U87MG cells treated with si-GPX4@IONPs at different I/S ratios (n = 3). (d) Agarose gel electrophoresis of free si-GPX4 and FA/si-GPX4@IONPs in the RNase degradation assay. (e) Pt release profile of FA/Pt+si-GPX4@IONPs in solutions with different pH values. (f) Dispersibility and stability of FA/Pt+si-GPX4@IONPs in PBS, culture medium with serum, and culture medium without serum (n = 3). Data are shown as the mean ± SE. One-way ANOVA was performed for multigroup comparisons: **p < 0.01 and ***p < 0.001.

Based on the negative charge and porous surface of our IONPs, Pt was loaded into the IONPs with a high loading amount of 15.56% and a 19.45% encapsulation efficiency. Interestingly, these FA/Pt+siGPX4@IONPs showed a pH-sensitive drug release profile (Figure 2e). After an incubation for 72 h, 29.4% and 23.1% of Pt was released from FA/Pt+si-GPX4@IONPs in a solution at pH 4 and 5.5 respectively, but only 12.7% at a pH of 7.4. The distinctive drug release profiles in solutions with different pH values are potentially attributed to the alteration of hydrogen bonds and electrostatic interactions.[39] To monitor dispersibility and stability of FA/Pt+si-GPX4@IONPs, we detected the hydrodynamic diameter in PBS, culture medium with and without serum for 6 days, the diameter did not change significantly, and PDI value is 0.030，0.035 and 0.044 respectively, which indicated that the FA/Pt+si-GPX4@IONPs were stable in above solution without further aggregation (Figure 2f, n = 3). Based on these results, IONPs with a porous structure may be potential carriers for the delivery of Pt and si-GPX4, may facilitate pH-sensitive drug release, and protect loaded siRNAs to achieve the desired effects.

**Biocompatibility and Selective Uptake of IONPs by Glioma Cells.** The natural next step in the process was to evaluate the uptake of our nanocarriers *in vitro*. The intracellular distribution of IONPs was examined in a human glioblastoma cell line (U87MG cells) and in NHAs after an incubation with our nanoparticles. As the nanoparticles are covered with Lipofectamine, fusion with the cell membrane is easily achieved and enables the release of si-GPX4 into the cytoplasm and the capture of the remaining parts of the nanoparticles by lysosomes. After an incubation with 100 µg/mL Pt-si-GPX4@IONPs and FA/Pt-si-GPX4@IONPs for 4 h, both NHAs and U87MG cells showed uptake of nanoparticles into the cytoplasm. The intracellular concentration of FA/Pt-si-GPX4@IONPs was higher than uncoated Pt+siGPX4@IONPs, likely due to the Lipofectamine and DSPE-PEG2K-FA coating (Figure 3a and b). Compared to NHAs, the U87MG cells generally showed higher uptake, likely due to higher expression of FOLR1 and FOLR2 (Figure 3b). TEM images showed lipid bilayer membrane vesicles encapsulating Pt-si-GPX4@IONPs and FA/Pt-si-GPX4@IONPs, and their contents were partially degraded (Figure 3a and b). Therefore, IONPs were degraded in the intracellular acidic environment of endosomes/lysosomes.

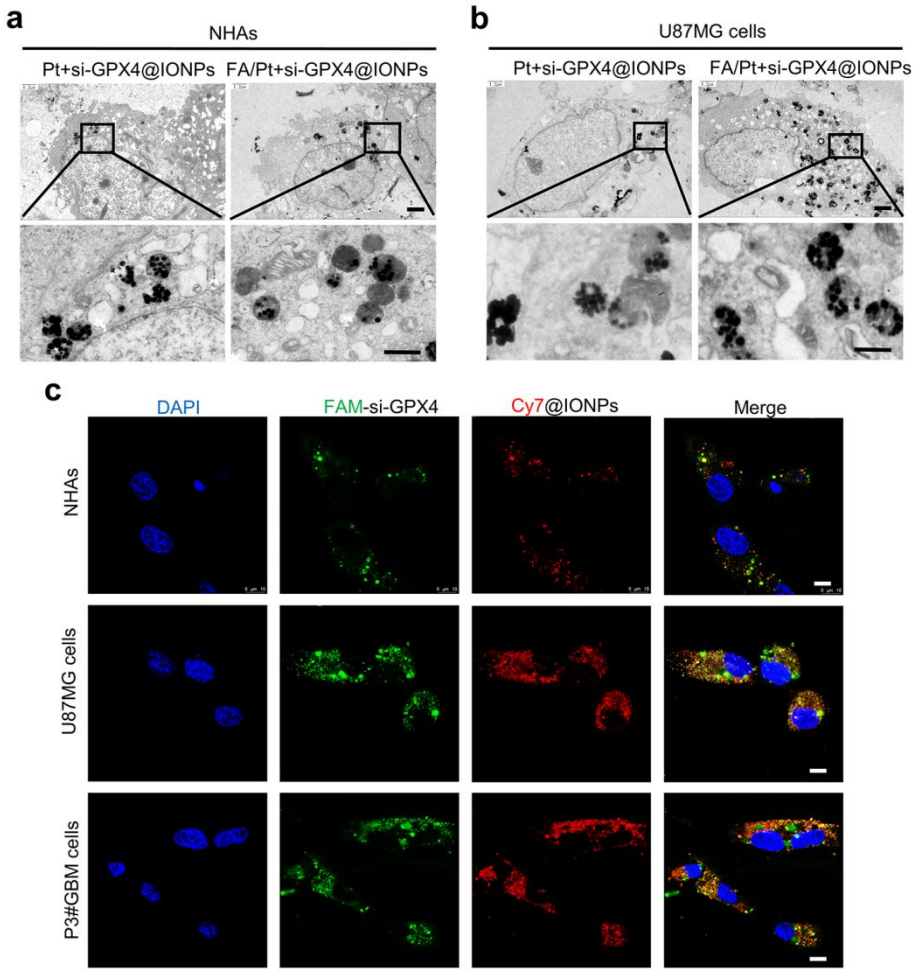


**Figure 3.** (a) TEM images of NHAs with internalized Pt+si-GPX4@IONPs and FA/Pt+si-GPX4@IONPs. The scale bar of the top image is 1.2 μm, and the scale bar of the bottom image is 0.6 μm. (b) TEM images of U87MG cells with internalized Pt+si-GPX4@IONPs and FA/Pt+si-GPX4@IONPs. The scale bar of the top image is 1.2 μm, and the scale bar of the bottom image is 0.6 μm. (c) Images of FA/Pt+si-GPX4@IONP endocytosis in NHAs, U87MG cells, and P3#GBM cells. The nuclei were stained with

DAPI (blue), si-GPX4 was labeled with FAM (green), and IONPs were coated with DSPE-PEG-Cy7 (red). Scale bar: 10 μm.

To further elucidate the uptake and distribution of FA/Pt-si-GPX4@IONPs intracellularly, FA/Pt-si-GPX4@IONPs were labeled with DSPE PEG2K-Cy7, Lipofectamine, and DSPE-PEG2K-FA at a molar ratio of 6:1:1. NHAs, U87MG cells, and P3#GBM cells were incubated with Cy7/FA/Pt-si-GPX4@IONPs for 4 h, and confocal microscopy images showed only partial colocalization (yellow) of the red and green (FAM-labeled si-GPX4) fluorescence; the remaining green fluorescence was dispersed in the cytoplasm, consistent with the TEM results. Thus, si-GPX4 was released into the cytoplasm before being captured by lysosomes. Compared to NHAs, the U87MG and P3#GBM cells exhibited higher red and green fluorescence intensities, which further explains the targeting characteristics of FA/Pt-si-GPX4@IONPs (Figure 3c).

**Therapeutic Effect of Nanodrugs *In Vitro.*** The antitumor effect of Pt/si-GPX4 coloaded IONPs *in vitro* was assessed using the CCK-8 assay. Cells were treated with free Pt, Pt-loaded IONPs (Pt@IONPs), si-GPX4-loaded IONPs (si-GPX4@IONPs), Pt- and si-

GPX4-loaded IONPs (Pt+si-GPX4@IONPs), and Lipofectamine- and FA-covered IONPs loaded with Pt and si-GPX4 (FA/Pt+si-GPX4@IONPs). The viability of U87MG cells decreased markedly after a 48 h incubation with Pt, Pt@IONPs, si-GPX4@IONPs, Pt+si-GPX4@IONPs, and FA/Pt+si-GPX4@IONPs. The most significant difference in cell viability was observed after the loading of 4 μg/mL Pt and 663 ng/mL si-GPX4. The viability of U87MG cells treated with Pt, Pt+si-GPX4@IONPs, and FA/Pt+si-GPX4@IONPs was 52.8%, 28.6%, and 13.6%, respectively. Interestingly, no significant difference in viability was observed between cells treated with Pt and cells treated with Pt@IONPs (Figure 4a, $p < 0.01$, $n = 3$). Cell viability assays in NHAs produced similar results, but intriguingly, no significant difference was observed between NHAs treated with Pt+si-GPX4@IONPs and with FA/Pt+si-GPX4@IONPs (Supplementary Figure 4a, $n = 3$). Since the FA/Pt+si-GPX4@IONPs showed an outstanding ability to kill GBM cells, the viability of U87MG cells, P3#GBM cells, and NHAs was also evaluated after treatment with FA/Pt+si-GPX4@IONPs. The cytotoxic effects of different concentrations of FA/Pt+si-GPX4@IONPs on NHAs were inappreciable after a 48 h incubation at concentrations ranging from 0-6.4 μg/mL, with cell viability greater than 80% (Figure 4b,

p < 0.05, n = 3). The viability of U87MG cells and P3#GBM cells was significantly decreased after treatment with these same concentrations. The viability of U87MG and P3#GBM cells decreased to 37.3% and 54.7%, respectively, when the concentration of the FA/Pt+si-GPX4@IONPs was 3.125 μg/mL. Based on these findings, our nanodrug displayed higher cytotoxicity in U87MG and P3#GBM cells than in NHAs.

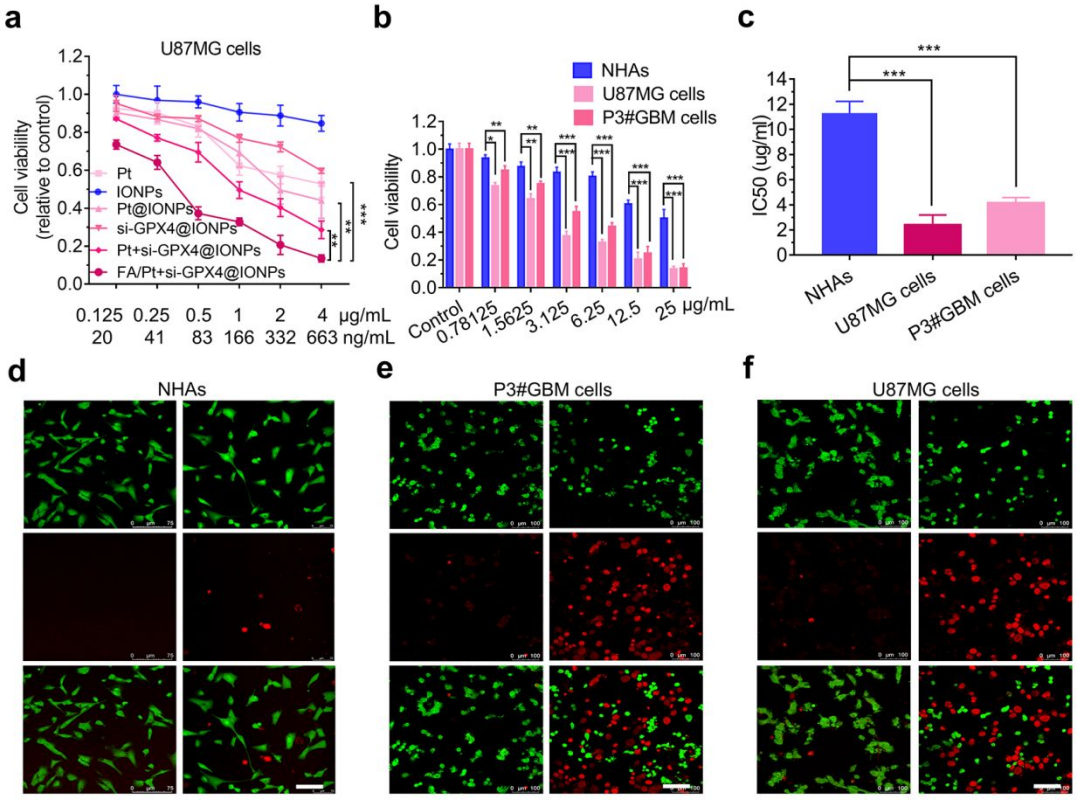


**Figure 4.** (a) Viability of U87MG cells after an incubation with different concentrations of the different nanoparticles and free Pt for 48 h (n = 3). (b) Cytotoxicity of FA/Pt+si-GPX4@IONPs in NHAs, U87MG cells and P3#GBM cells after an incubation for 48 h (n

= 3). (c) Half maximal inhibitory concentrations (IC50s) of FA/Pt+si-GPX4@IONPs in NHAs compared with U87MG and P3#GBM cells (n = 3). (d) Confocal microscopy images of Live/Dead staining of NHAs treated with 4 μg/mL FA/Pt+si-GPX4@IONPs after 48 h. Scale bar: 100 μm. (e) Confocal microscopy images of Live/Dead staining of P3#GBM cells treated with 4 μg/mL FA/Pt+si-GPX4@IONPs after 48 h. Scale bar: 100 μm. (f) Confocal microscopy images of Live/Dead staining of U87MG cells treated with 4 μg/mL FA/Pt+si-GPX4@IONPs after 48 h. Scale bar: 100 μm. Data are shown as the mean ± SE. One-way ANOVA for multigroup comparisons: *$p < 0.05$, **$p < 0.01$, and ***$p < 0.001$.

Glioma cells exhibit higher rates of endocytosis and active cellular metabolism, higher levels of D-glucose, and produce greater amounts of $H_2O_2$ than normal brain cells. These characteristics might explain why FA/Pt+si-GPX4@IONPs more readily induce cytotoxicity in glioma cells.[40] The IC50 of FA/Pt+si-GPX4@IONPs nanoparticles in U87MG and P3#GBM cells was 2.37 μg/mL and 4.13 μg/mL, respectively, values that were significantly lower than the value of 11.29 μg/mL in NHAs (Figure 4c, $p < 0.001$, n

= 3). Based on this finding, we concluded that our nanodrug is sufficiently cytotoxic in glioma cells but does not induce the same level of cytotoxicity in the surrounding brain tissue.

Live/Dead cell viability assays were performed to elucidate the death rate of U87MG cells, P3#GBM cells, and NHAs treated with FA/Pt+si-GPX4@IONPs. Live cells, which were indicated by green fluorescence, and dead cells, which showed red fluorescence, were identified using confocal laser scanning microscopy. Therefore, both apoptotic and ferroptotic cells were stained red. The confocal microscopy results did not reveal a significant increase in the cell death rate of NHAs after an incubation with 4 µg/mL FA/Pt+si-GPX4@IONPs (Figure 4d). Importantly, the death rates of U87MG and P3#GBM cells were 52.5% and 56.9%, respectively, indicating that the nanoparticles were more toxic to U87MG and P3#GBM cells than to NHAs (Figure 4e and f and Supplementary Figure 4b, n = 3). These results confirm the results of the CCK-8 assay showing that FA/Pt+si-GPX4@IONPs are more toxic to glioma (U87MG and P3#GBM) cells than to normal brain tissue (NHAs).

**Pt-loaded IONPs Induce Apoptosis.** Pt is a widely used treatment for various cancers. The antitumor mechanism of Pt involves three different pathways. First, Pt crosslinks DNA bases in the nucleus to cause DNA damage and disrupt DNA replication and transcription. Second, Pt induces mitochondrial DNA damage. Both DNA damage and mitochondrial DNA damage cause tumor cell apoptosis. Finally, Pt activates NOX, NOX converts NADPH to NADP+ to release electrons, generate $O_2^-$, and participate in $H_2O_2$ formation (Figure 5a). We performed an Annexin V-FITC/PI assay using flow cytometry to analyze apoptosis (Figure 5b and Supplementary Figure 4c). At a concentration of 4 μg/mL, free Pt initiated an apoptotic response in approximately 6% of U87MG cells after a 48 h incubation. Once the IONPs were applied as carriers for Pt, the ratio of apoptotic U87MG cells increased, likely due to the high rate of endocytosis. The apoptosis rates of U87MG cells exposed to Pt@IONPs, Pt+si-GPX4@IONPs, and FA/Pt+si-GPX4@IONPs at a concentration of 4 μg/mL were 24.0%, 26.6%, and 33.3%, respectively.

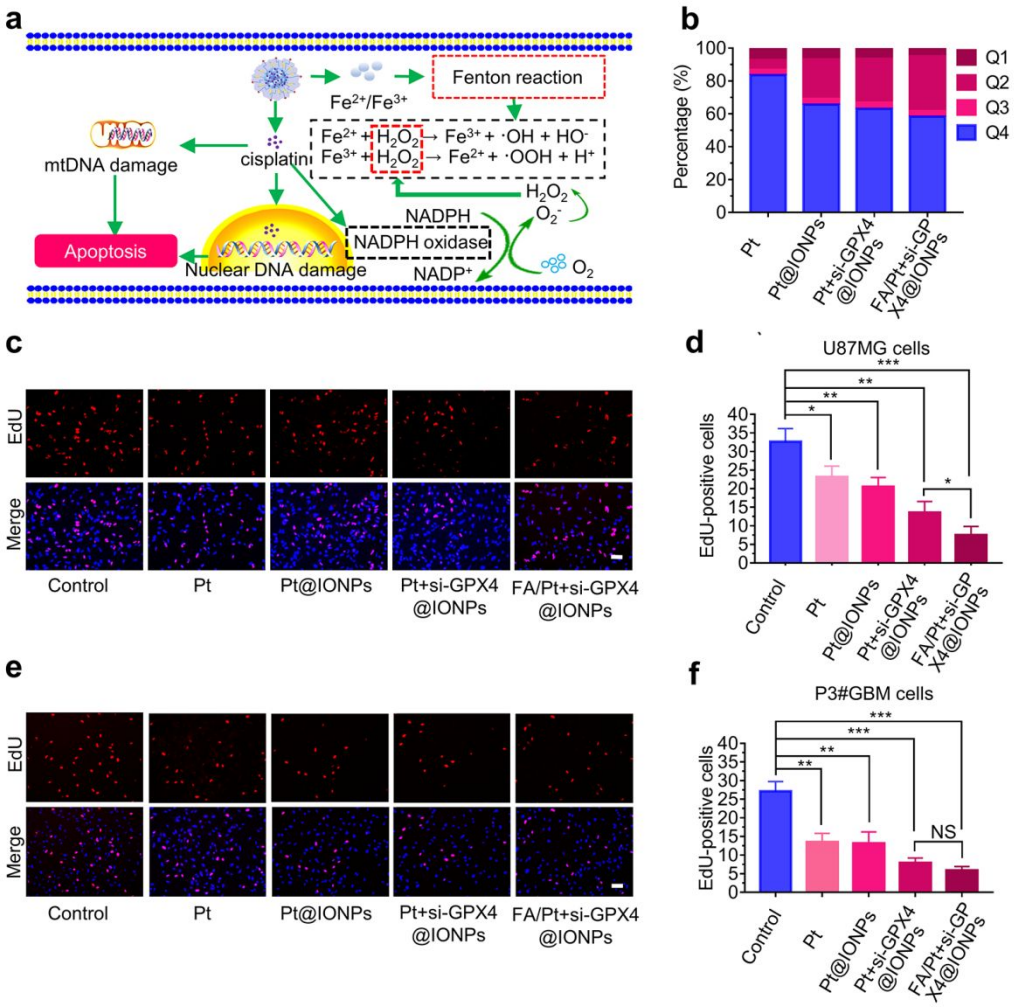


**Figure 5.** (a) Schematic illustrating the mechanism of action of Pt in glioblastoma cells. (b) Statistical results of flow cytometry analysis of apoptosis of U87MG cells after treatment with IONPs, Pt@IONPs, Pt+si-GPX4@IONPs, and FA/Pt+si-GPX4@IONPs for 48 h. (c) The proliferation rate of U87MG cells treated with PBS, Pt, Pt@IONPs, Pt+si-GPX4@IONPs, and FA/Pt+si-GPX4@IONPs for 48 h, as measured using the EdU (red) assay. The nuclei were stained with DAPI (blue). Scale bar: 100 μm. (d)

Graphical representation of the ratios of EdU-positive U87MG cells treated with PBS, Pt, Pt@IONPs, Pt+si-GPX4@IONPs, and FA/Pt+si-GPX4@IONPs (n = 3). (e) The proliferation rate of P3#GBM cells treated with PBS, Pt, Pt@IONPs, Pt+si-GPX4@IONPs, and FA/Pt+si-GPX4@IONPs for 48 h, as measured using the EdU (red) assay. The nuclei were stained with DAPI (blue). Scale bar: 100 μm. (f) Graphical representation of the ratios of EdU-positive P3#GBM cells treated with PBS, Pt, Pt@IONPs, Pt+si-GPX4@IONPs, and FA/Pt+si-GPX4@IONPs (n = 3). Data are shown as the mean ± SE. One-way ANOVA was used for multigroup comparisons: NS = nonsignificant, *$p < 0.05$, **$p < 0.01$, and ***$p < 0.001$.

We performed an EdU assay, which can effectively detect the percentage of cells currently in the S phase of mitosis, to evaluate the proliferation of glioblastoma cells exposed to our nanodrugs. EdU inserts into DNA molecules that are replicating as cells proliferate. Reactions between EdU and the DNA produce red fluorescence, which was visualized using confocal laser scanning microscopy. Compared to control cells, the proliferation of U87MG cells treated with Pt, Pt@IONPs, si-GPX4@IONPs, Pt+si-

GPX4@IONPs, and FA/Pt+si-GPX4@IONPs was significantly inhibited after a 48 h incubation. A noticeable difference in the inhibition of proliferation was observed between U87MG cells incubated with Pt+si-GPX4@IONPs and with FA/Pt+si-GPX4@IONPs (Figure 5c and d, $p < 0.05$, $n = 3$). Similar results were observed for P3#GBM cells, with the same difference in inhibition observed between P3#GBM cells incubated with FA-coated nanoparticles and cells incubated with noncoated nanoparticles (Figure 5e and f, $p < 0.05$, $n = 3$). Taken together, these results confirmed that our Pt-loaded nanoparticles inhibited proliferation and induced apoptosis in human glioblastoma cells, with FA/Pt+si-GPX4@IONPs identified as the most efficient experimental particles.

**The Combination of si-GPX4 with IONPs Induces Ferroptosis.** GPX4 is a unique intracellular antioxidant enzyme that regulates ferroptosis by directly reducing lipid peroxidation at the expense of reducing GSH into GSSG, contributing to protecting the cell from oxidative stress.[41] As a result, the depletion of GPX4 causes the accumulation of lipid peroxidation products (Figure 6a). Firstly, we analyzed the iron release profile after an incubation for 12h, $Fe^{2+}/Fe^{3+}$ concentration was 0.129 μg/mL, 0.041 μg/mL and

0.006 μg/mL at pH 4, 5.5, 7.4, respectively (Supplementary Figure 5a, $p < 0.05$, $n = 3$). The generation of hydroxyl radicals was also identified with $Fe^{2+}/Fe^{3+}$ concentration after adding 10% $H_2O_2$ (Supplementary Figure 5b, $p < 0.05$, $n = 3$).

GPX4 knockdown increases the levels of lipid peroxidation products, leading to ferroptosis.[42] In our study, we loaded si-GPX4 into IONPs to knockdown GPX4 expression. As shown in Figure 6b, after treatment with 4 μg/mL FA/Pt+si-GPX4@IONPs (663 ng/mL) for 48 h, the expression of the GPX4 protein (green fluorescence) was detected in NHAs, U87MG cells, and P3#GBM cells using immunofluorescence staining. In all three cell lines, GPX4 expression was significantly decreased in cells treated with FA/Pt+si-GPX4@IONPs compared to control, PBS-treated cells. Statistical models showed a slightly lower level of endogenous GPX4 expression in NHAs than that in U87MG and P3#GBM cells. In U87MG and P3#GBM cells, GPX4 levels decreased to 30.9% and 36.4% of the original levels, respectively, after the FA/Pt+si-GPX4@IONPs treatment for 48 h (Figure 6c, $n = 3$). In conclusion, the inclusion of si-GPX4 in our FA/Pt+si-GPX4@IONPs significantly inhibited the expression of GPX4 in glioblastoma cell lines.

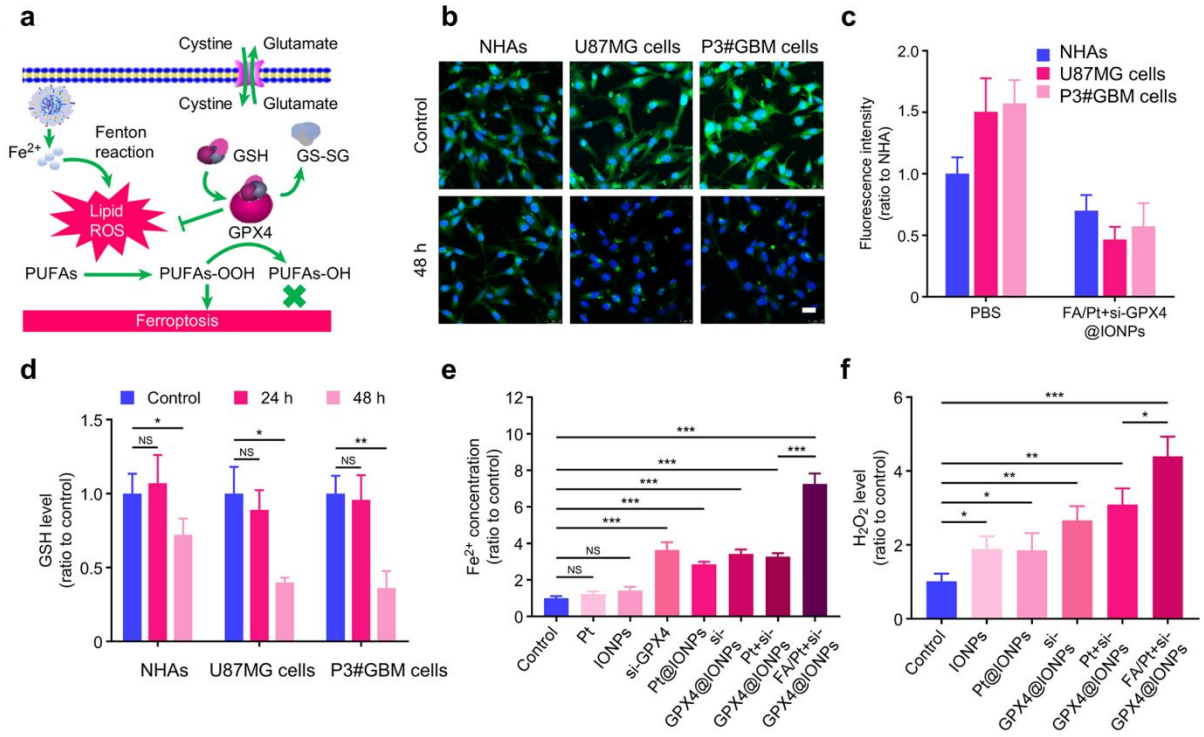


**Figure 6.** (a) Schematic illustrating the mechanism of ferroptosis in FA/Pt+si-GPX4@IONP-treated glioblastoma cells. (b) GPX4 expression (green) in NHAs, U87MG cells and P3#GBM cells treated with FA/Pt+si-GPX4@IONPs for 48 h. The nuclei were stained with DAPI (blue). Scale bar: 25 μm. (c) Corresponding quantitative analysis of the green fluorescence intensity (n = 3). (d) GSH levels in NHAs, U87MG cells and P3#GBM cells treated with FA/Pt+si-GPX4@IONPs for 48 h (n = 3). (e) $Fe^{2+}$ concentrations in U87MG cells exposed to different treatments for 48 h (n = 3). (f) $H_2O_2$ levels in P3#GBM cells exposed to different treatments for 48 h (n = 3). Data are shown

as the mean ± SE. One-way ANOVA was used for multigroup comparisons: NS = nonsignificant, *$p < 0.05$, **$p < 0.01$, and ***$p < 0.001$.

In our model, we used IONP nanocarriers to increase intracellular iron ($Fe^{2+}$ and $Fe^{3+}$) concentrations, which triggered Fenton reactions with the $H_2O_2$ produced by Pt. Furthermore, the generated ROS (particularly lethal hydroxyl radicals) degraded polyunsaturated fatty acids (PUFAs) into PUFA-OOH, a hallmark of ferroptosis. Because GPX4 plays an integral role in inhibiting ferroptosis, si-GPX4 should exert measurable effects *in vitro*. GSH is the substrate of GPX4 and therefore a marker of GPX4 function. Therefore, we analyzed intracellular GSH levels using GSH and GSSG assay kits (Figure 6d, n = 3). The level of GSH was not altered significantly in glioblastoma cells or NHAs after an incubation with 4 μg/mL FA/Pt+si-GPX4@IONPs for 24 h. However, GSH levels were substantially reduced in U87MG and P3#GBM cells after a 48 h incubation. This finding might be explained by the ubiquitous expression of GSH in cells and its various other functions, such as roles as an antioxidant and in detoxification. Additionally, the expenditure of GSH induced by the FA/Pt+si-

GPX4@IONP treatment consumes much more GSH than the amount saved by GPX4 knockdown.

As ferrous iron ($Fe^{2+}$) plays a key role in ferroptosis, we next assessed the intracellular $Fe^{2+}$ level in U87MG cells after a 48 h incubation with 4 µg/mL FA/Pt+si-GPX4@IONPs (Figure 6e, n = 3). The same experiment was performed in P3#GBM cells (Supplementary Figure 5c, n = 3). Compared to the control treatment (Pt and si-GPX4), the incubation with IONPs increased the $Fe^{2+}$ concentration by approximately 3-4-fold. Importantly, FA/Pt+si-GPX4@IONPs distinctly increased $Fe^{2+}$ concentrations by a factor of 7.25 in U87MG cells and by a factor of 7.9 in P3#GBM cells relative to control levels. $H_2O_2$ levels were also analyzed in U87MG and P3#GBM cells after treatment with our nanoparticles (Figure 6f and Supplementary Figure 5d, $p < 0.05$, n = 3). FA/Pt+si-GPX4@IONPs dramatically increased intracellular $H_2O_2$ levels. As the detection of intracellular superoxide anion concentrations is important to assess ferroptosis induction, a superoxide probe, DHE, was used. As shown in Supplementary Figure 5e, red fluorescence was significantly stronger in cells treated with Pt- and si-GPX4-loaded nanoparticles than in unloaded nanoparticles. Cells treated with FA/Pt+si-

GPX4@IONPs nanoparticles presented the strongest red fluorescence, suggesting that these nanoparticles were the most effective at increasing superoxide levels.

Ferroptosis is characterized by lipid peroxidation, and the final product of lipid peroxidation, MDA, was detected using a lipid peroxidation MDA assay kit.[43,44,451]U87MG cells were incubated with the different nanoparticles for 48 h, and MDA levels were significantly increased in cells treated with si-GPX4@IONPs, Pt+si-GPX4@IONPs, and FA/Pt+si-GPX4@IONPs, which exhibited MDA levels that were 7.76, 2.96 and 4.05 times the control MDA levels, respectively. The MDA level in U87MG cells treated with FA/Pt+si-GPX4@IONPs was 1.38 times higher than in U87MG cells treated with Pt+si-GPX4@IONPs (Supplementary Figure 5f, $p < 0.05$, $n = 3$). Thus, our nanodrug was efficient at reducing the level of the GPX4 protein and increasing the intracellular iron levels through the interaction between Pt and si-GPX4, which induced ferroptosis in glioblastoma cells.

***In Vivo* Cancer Therapy.** The *in vivo* efficacy of our Pt- and si-GPX4-coloaded IONPs against glioblastoma was investigated in immune-deficient nude mice bearing luciferase-labeled U87MG orthotopic xenografts. Seven days after tumor initiation, the

*in situ* tumor models were divided into five groups (n = 10 mice per group): 1) the control group, which was injected with saline, 2) the free Pt-treated group, 3) the Pt@IONP-treated group, 4) the Pt+si-GPX4@IONP-treated group, and 5) the FA/Pt+si-GPX4@IONP-treated group. All injections were carried out with the aid of a stereotactic instrument. The dose of nanoparticles administered to all groups was 4 μg/mL, with a volume of 4 μL per injection. Six injections were performed over 12 days. Figure 6a shows the schedule of the *in vivo* treatments. BLI was used to monitor the tumor size from days 0 to 12. The intensity of the bioluminescence signal (radiance) was quantified under the same conditions (Figure 7a). Similar to the *in vitro* results, FA/Pt+si-GPX4@IONPs showed the strongest tumor inhibitory effect of the 5 treatments (Figure 7b). During therapy, the tumors of mice in the saline-treated control group grew extensively, while the tumors of mice in the free Pt-treated group showed a slight inhibition of growth. Compared to Pt, Pt@IONPs and Pt+si-GPX4@IONPs showed even greater abilities to suppress tumor growth, while FA/Pt+si-GPX4@IONPs exhibited the greatest effect on inhibiting tumor growth and induced the lowest level of tumor bioluminescence (Figure 7c, n = 10). A Kaplan-Meier analysis of the survival data

showed that the overall survival times were 16.9 days, 18.5 days, 20.7 days, 27.4 days, and more than 38.3 days for animals in the saline-, free Pt-, Pt@IONP-, Pt+si-GPX4@IONP-, and FA/Pt+si-GPX4@IONP-treated groups, respectively (Figure 7d, n = 10). During the 12 days of treatment, no obvious body weight changes were observed among the Pt@IONP-, Pt+si-GPX4@IONP-, and FA/Pt+si-GPX4@IONP-treated groups (Figure 7e, n = 10). However, the body weights of mice in the saline- and Pt-treated groups were altered, likely due to the uninhibited tumor growth that induced disturbances in brain functions affecting eating and resting behavior. IHC staining for Ki-67 was performed in mouse brain tumor samples to investigate changes in proliferation induced by different GPX4 levels (Figure 7f). Ki-67 expression in all experimental groups treated with different nanoparticles was significantly suppressed compared to the saline group. The FA/Pt+si-GPX4@IONP-treated group exhibited the lowest number of Ki-67-positive cells, indicating that cell proliferation was significantly inhibited *in vivo.* IHC staining for GPX4 also revealed decreased expression in the FA/Pt+si-GPX4@IONP-treated group and a less robust decrease in the Pt+si-GPX4@IONP-treated group (Supplementary Figure 6a). H&E staining was also performed in tumor

samples and the major organs, i.e., the heart, liver, spleen, lung, and kidney (Supplementary Figure 6b). H&E staining showed the largest area of cell death within tumor samples from mice treated with FA/Pt+si-GPX4@IONPs, with no noticeable cell death in the major organs. In summary, the combination of apoptosis and ferroptosis allowed FA/Pt+si-GPX4@IONPs nanoparticles to exert a significant effect on glioblastoma *in vivo* without causing noticeable damage to the vital organs.

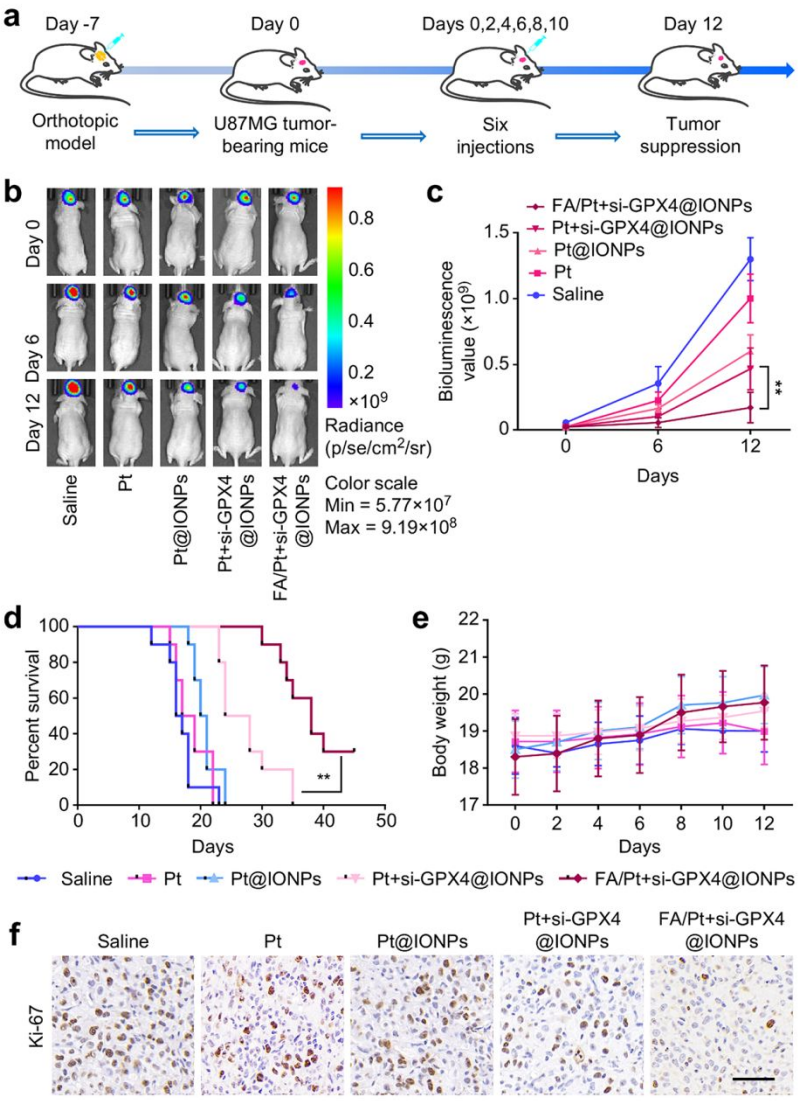


**Figure 7.** (a) Experimental schedule of the *in vivo* treatments. (b) Intracranial tumor growth of the BLI of luciferase-expressing U87MG cells monitored 0, 6, and 12 days using the IVIS-200 imaging system. (c) Quantification of the bioluminescence in orthotopic tumor-bearing mice (n = 10). (d) Overall survival was determined by constructing Kaplan-Meier survival curves, and a log-rank test was used to assess the

statistical significance of the differences (n = 10). (e) Changes in the body weight of mice during the treatment process (n = 10). (f) Representative images of IHC staining for Ki67 in mouse brain sections. Scale bar: 50 μm. Data are shown as the mean ± SE. One-way ANOVA was used for multigroup comparisons: *$p < 0.05$, **$p < 0.01$, and ***$p < 0.001$.

## CONCLUSIONS

In our study, we successfully constructed gene therapy-based IONPs for the treatment of glioblastoma by inducing a combination of ferroptosis and apoptosis. Our synthesized FA/Pt+si-GPX4@IONPs were prepared using a moderate triple on-demand reaction and coated with Lipofectamine to protect the loaded si-GPX4 from degradation. The surface of the nanodrug, which showed selective glioblastoma cell targeting characteristics *in vitro* and *in vivo,* was modified with encapsulated FA. Three main components enabling two pathways of attack, namely, Pt, si-GPX4, and the IONPs themselves, were included in our nanodrug. The IONPs entered cells, were degraded, and induced increased intracellular levels of $Fe^{2+}$ and $Fe^{3+}$. Pt degraded both nuclear

DNA and mitochondrial DNA, leading to apoptosis and simultaneously producing $H_2O_2$. These changes laid the foundation for efficient production of ROS (notably hydroxyl radicals) through the Fenton reaction as a result of increased levels of intracellular reactants ($Fe^{2+}$, $Fe^{3+}$, and $H_2O_2$). GPX4, a key negative regulator of the ferroptotic process, was synchronously knocked down by co-loading si-GPX4, increasing the extent of ferroptosis initiation. Our study describes a novel nanomedicine for the treatment of glioblastoma aimed at combining the processes of ferroptosis and apoptosis to increase antitumor effects. Furthermore, the drug produced few side effects, enabling potential clinical implementation in postoperative patients. Taken together, our results provide a foundation for the development of highly efficient, multipurpose, and bio-safe “ferroapoptotic” glioblastoma therapies.

## ASSOCIATED CONTENT

### Supporting Information

qRT-PCR analysis and viability of NHAs, U87MG cells, and P3#GBM cells infected with two independent GPX4 siRNAs. FOLR1 and FOLR2 mRNA expression in GBM and

LGG cells determined from the GEPIA database. Western blot analysis of levels of the FOLR1 and FOLR2 proteins in NHAs, U87MG cells, and P3#GBM cells. TEM image of si-GPX4@IONPs. Celll viability of NHAs after an incubation with different nanoparticles. Cell death rates of NHAs, U87MG cells, and P3#GBM cells exposed to different treatments for 48 h. $Fe^{2+}$ concentrations, $H_2O_2$ levels, and MDA levels in U87MG cells exposed to the different treatments. Representative images of DHE in U87MG cells treated with different nanoparticles. IHC staining for GPX4 in sections from mouse brains. H&E-stained sections from heart, liver, kidney, spleen, and lung of tumor-bearing mice.

AUTHOR INFORMATION

***Corresponding Author**

Shilei Ni

Associate Professor of Neurosurgery Department, Qilu Hospital of Shandong University, 107 Wenhua Xi Road, Jinan, Shandong 250012, P.R. China

Telephone: +8613869196590

E-mail: nishilei@sdu.edu.cn

Funding Sources

The study was supported by grants from the National Natural Science Foundation of China [grant numbers 81874082, 81472353 and 81502148], the Key Research and Development Plan of Shandong Province [grant numbers 2016GSF201014 and 2018GSF118094], the Shandong Provincial Natural Science Foundation [grant number ZR2015HM074], and the Jinan Science and Technology Development Plan [grant number 201821049].

## Notes

The authors have no conflicts of interest to declare.

ACKNOWLEDGMENTS

We would like to acknowledge the technical support received from Shandong University Structural Constituent and Physical Property Research Facilities/SDU SC&PP Research Facilities.

## REFERENCES

(1) Stupp, R.; Hegi, M. E.; Mason, W. P.; Van den Bent, M. J.; Taphoorn, M. J.; Janzer, R. C.; Ludwin, S. K.; Allgeier, A.; Fisher, B.; Belanger, K.; Hau, P.; Brandes, A. A.; Gijtenbeek, J.; Marosi, C.; Vecht, C. J.; Mokhtari, K.; Wesseling, P.; Villa, S.; Eisenhauer, E.; Gorlia, T.; Weller, M.; Lacombe, D.; Cairncross, J. G.; Mirimanoff, R. O. Effects of Radiotherapy with Concomitant and Adjuvant Temozolomide Versus Radiotherapy Alone on Survival in Glioblastoma in a Randomised Phase III Study: 5-Year Analysis of the EORTC-NCIC Trial. *Lancet Oncol.* **2009**, *10*, 459–466.

(2) Stupp, R.; Mason, W. P.; Van den Bent, M. J.; Weller, M.; Fisher, B.; Taphoorn, M. J.; Belanger, K.; Brandes, A. A.; Marosi, C.; Bogdahn, U.; Curschmann, J.; Janzer, R. C.; Ludwin, S. K.; Gorlia, T.; Allgeier, A.; Lacombe, D.; Cairncross, J. G.; Eisenhauer, E.; Mirimanoff, R. O. Radiotherapy Plus Concomitant and Adjuvant Temozolomide for Glioblastoma. *N. Engl. J. Med.* **2005**, *352*, 987–996.

(3) Park, J. K.; Hodges, T.; Arko, L.; Shen, M.; Iacono, D.; McNabb, A.; Bailey, N. O.; Kreisl, T. N.; Iwamoto, F. M.; Sul, J.; Auh, S.; Park, G. E.; Fine, H. A.; Black, P. M. Scale

to Predict Survival after Surgery for Recurrent Glioblastoma Multiforme. *J. Clin. Oncol.* **2010**, *28*, 3838–3843.

(4) Gilbert, M. R.; Dignam, J. J.; Armstrong, T. S.; Wefel, J. S.; Blumenthal, D. T.; Vogelbaum, M. A.; Colman, H.; Chakravarti, A.; Pugh, S.; Won, M.; Jeraj, R.; Brown, P. D.; Jaeckle, K. A.; Schiff, D.; Stieber, V. W.; Brachman, D. G.; Werner-Wasik, M.; Tremont-Lukats, I. W.; Sulman, E. P.; Aldape, K. D.; Curran, W. J., Jr.; Mehta, M. P. A Randomized Trial of Bevacizumab for Newly Diagnosed Glioblastoma. *N. Engl. J. Med.* **2014**, *370*, 699–708.

(5) Spiteri, I.; Caravagna, G.; Cresswell, G. D.; Vatsiou, A.; Nichol, D.; Acar, A.; Ermini, L.; Chkhaidze, K.; Werner, B.; Mair, R.; Brognaro, E.; Verhaak, R. G. W.; Sanguinetti, G.; Piccirillo, S. G. M.; Watts, C.; Sottoriva, A. Evolutionary Dynamics of Residual Disease in Human Glioblastoma. *Ann. Oncol.* **2019**, *30*, 456–463.

(6) Otani, Y.; Ichikawa, T.; Kurozumi, K.; Inoue, S.; Ishida, J.; Oka, T.; Shimizu, T.; Tomita, Y.; Hattori, Y.; Uneda, A.; Matsumoto, Y.; Michiue, H.; Date, I. Fibroblast Growth Factor 13 Regulates Glioma Cell Invasion and is Important for Bevacizumab-Induced Glioma Invasion. *Oncogene* **2018**, *37*, 777–786.

(7) Westphal, M.; Lamszus, K. The Neurobiology of Gliomas: From Cell Biology to the Development of Therapeutic Approaches. *Nat. Rev. Neurosci.* **2011**, *12*, 495–508.

(8) Oddo, A.; Peng, B.; Tong, Z.; Wei, Y.; Tong, W. Y.; Thissen, H.; Voelcker, N. H. Advances in Microfluidic Blood-Brain Barrier (BBB) Models. *Trends in biotechnology.* **2019**, *37*, 1295-1314.

(9) Lorch, J. H.; Goloubeva, O.; Haddad, R. I.; Cullen, K.; Sarlis, N.; Tishler, R.; Tan, M.; Fasciano, J.; Sammartino, D. E.; Posner, M. R. Induction Chemotherapy with Cisplatin and Fluorouracil Alone or in Combination with Docetaxel in Locally Advanced Squamous-Cell Cancer of the Head and Neck: Long-Term Results of the TAX 324 Randomised Phase 3 Trial. *Lancet Oncol.* **2011**, *12*, 153–159.

(10) Long, D.; Liu, T.; Tan, L.; Shi, H.; Liang, P.; Tang, S.; Wu, Q.; Yu, J.; Dou, J.; Meng, X. Multisynergistic Platform for Tumor Therapy by Mild Microwave Irradiation-Activated Chemotherapy and Enhanced Ablation. *ACS Nano* **2016**, *10*, 9516–9528.

(11) Friedman, H. S.; Prados, M. D.; Wen, P. Y.; Mikkelsen, T.; Schiff, D.; Abrey, L. E.; Yung, W. K.; Paleologos, N.; Nicholas, M. K.; Jensen, R.; Vredenburgh, J.; Huang, J.;

Zheng, M.; Cloughesy, T. Bevacizumab alone and in Combination with Irinotecan in Recurrent Glioblastoma. *J. Clin. Oncol.* **2009**, *27*, 4733–4740.

(12) Tong, W. Y.; Alnakhli, M.; Bhardwaj, R.; Apostolou, S.; Sinha, S.; Fraser, C.; Kuchel, T.; Kuss, B.; Voelcker, N. H. Delivery of siRNA in vitro and in vivo using PEI-capped porous silicon nanoparticles to silence MRP1 and inhibit proliferation in glioblastoma. *Journal of nanobiotechnology.* **2018**, *16*, 1-17.

(13) Bogdan, A. R.; Miyazawa, M.; Hashimoto, K.; Tsuji, Y. Regulators of Iron Homeostasis: New Players in Metabolism, Cell Death, and Disease. *Trends Biochem. Sci.* **2016**, *41*, 274–286.

(14) Shen, Z.; Song, J.; Yung, B. C.; Zhou, Z.; Wu, A.; Chen, X. Emerging Strategies of Cancer Therapy Based on Ferroptosis. *Adv. Mater.* **2018**, *30*, e1704007.

(15) Zheng, D. W.; Lei, Q.; Zhu, J. Y.; Fan, J. X.; Li, C. X.; Li, C.; Xu, Z.; Cheng, S. X.; Zhang, X. Z. Switching Apoptosis to Ferroptosis: Metal-Organic Network for High-Efficiency Anticancer Therapy. *Nano Lett.* **2017**, *17*, 284–291.

(16) Zhou, X.; Zhang, Y.; Wang, C.; Wu, X.; Yang, Y.; Zheng, B.; Wu, H.; Guo, S.; Zhang, J. Photo-Fenton Reaction of Graphene Oxide: A New Strategy to Prepare Graphene Quantum Dots for DNA Cleavage. *ACS Nano* **2012**, *6*, 6592–6599.

(17) Zhang, C.; Bu, W.; Ni, D.; Zhang, S.; Li, Q.; Yao, Z.; Zhang, J.; Yao, H.; Wang, Z.; Shi, J. Synthesis of Iron Nanometallic Glasses and Their Application in Cancer Therapy by a Localized Fenton Reaction. *Angew. Chem. Int. Ed. Engl.* **2016**, *55*, 2101–2106.

(18) Yang, W. S.; Stockwell, B. R. Ferroptosis: Death by Lipid Peroxidation. *Trends Cell Biol.* **2016**, *26*, 165–176.

(19) Meng, H.; Xue, M.; Xia, T.; Ji, Z.; Tarn, D. Y.; Zink, J. I.; Nel, A. E. Use of Size and a Copolymer Design Feature to Improve the Biodistribution and the Enhanced Permeability and Retention Effect of Doxorubicin-Loaded Mesoporous Silica Nanoparticles in a Murine Xenograft Tumor Model. *ACS Nano* **2011**, *5*, 4131–4144.

(20) Yang, G.; Wang, J.; Wang, Y.; Li, L.; Guo, X.; Zhou, S. An Implantable Active-Targeting Micelle-in-Nanofiber Device for Efficient and Safe Cancer Therapy. *ACS Nano* **2015**, *9*, 1161–1174.

(21) Byrne, J. D.; Betancourt, T.; Brannon-Peppas, L. Active Targeting Schemes for Nanoparticle Systems in Cancer Therapeutics. *Adv. Drug Delivery Rev.* **2008**, *60*, 1615–1626.

(22) Zanganeh, S.; Hutter, G.; Spitler, R.; Lenkov, O.; Mahmoudi, M.; Shaw, A.; Pajarinen, J. S.; Nejadnik, H.; Goodman, S.; Moseley, M.; Coussens, L. M.; Daldrup-Link, H. E. Iron Oxide Nanoparticles Inhibit Tumour Growth by Inducing Pro-Inflammatory Macrophage Polarization in Tumour Tissues. *Nat Nanotechnol.* **2016**, *11*, 986–994.

(23) Dixon, S. J.; Lemberg, K. M.; Lamprecht, M. R.; Skouta, R.; Zaitsev, E. M.; Gleason, C. E.; Patel, D. N.; Bauer, A. J.; Cantley, A. M.; Yang, W. S.; Morrison, B., 3rd; Stockwell, B. R. Ferroptosis: An Iron-Dependent form of Nonapoptotic Cell death. *Cell* **2012**, *149*, 1060–1072.

(24) Huo, M.; Wang, L.; Wang, Y.; Chen, Y.; Shi, J. Nanocatalytic Tumor Therapy by Single-Atom Catalysts. *ACS Nano* **2019**, *13*, 2643–2653.

(25) Tassa, C.; Shaw, S. Y.; Weissleder, R. Dextran-Coated Iron Oxide Nanoparticles: A Versatile Platform for Targeted Molecular Imaging, Molecular Diagnostics, and Therapy. *Acc. Chem. Res.* **2011**, *44*, 842–852.

(26) Bose, R. J. C.; Kumar, S. U.; Zeng, Y.; Afjei, R.; Robinson, E.; Lau, K.; Bermudez, A.; Habte, F.; Pitteri, S. J.; Sinclair, R.; Willmann, J. K.; Massoud, T. F.; Gambhir, S. S.; Paulmurugan, R. Tumor Cell-Derived Extracellular Vesicle-Coated Nanocarriers: An Efficient Theranostic Platform for the Cancer-Specific Delivery of Anti-miR-21 and Imaging Agents. *ACS Nano* **2018**, *12*, 10817–10832.

(27) Trujillo-Alonso, V.; Pratt, E. C.; Zong, H.; Lara-Martinez, A.; Kaittanis, C.; Rabie, M. O.; Longo, V.; Becker, M. W.; Roboz, G. J.; Grimm, J.; Guzman, M. L. FDA-Approved Ferumoxytol Displays Anti-Leukaemia Efficacy Against Cells with Low Ferroportin Levels. *Nat. Nanotechnol.* **2019**, *14*, 616–622.

(28) Bulte, J. W. M. Superparamagnetic Iron Oxides as MPI Tracers: A Primer and Review of Early Applications. *Adv. Drug Delivery Rev.* **2019**, *138*, 293–301.

(29) Chee, H. L.; Gan, C. R. R.; Ng, M.; Low, L.; Fernig, D. G.; Bhakoo, K. K.; Paramelle, D. Biocompatible Peptide-Coated Ultrasmall Superparamagnetic Iron Oxide

Nanoparticles for *In vivo* Contrast-Enhanced Magnetic Resonance Imaging. *ACS Nano* **2018**, *12*, 6480–6491.

(30) Cardarelli, F.; Digiacomo, L.; Marchini, C.; Amici, A.; Salomone, F.; Fiume, G.; Rossetta, A.; Gratton, E.; Pozzi, D.; Caracciolo, G. The Intracellular Trafficking Mechanism of Lipofectamine-Based Transfection Reagents and Its Implication for Gene Delivery. *Sci. Rep.* **2016**, *6*, 25879.

(31) Vukovic, L.; Khatib, F. A.; Drake, S. P.; Madriaga, A.; Brandenburg, K. S.; Kral, P.; Onyuksel, H. Structure and Dynamics of Highly PEG-Ylated Sterically Stabilized Micelles in Aqueous Media. *J. Am. Chem. Soc.* **2011**, *133*, 13481–13488.

(32) Hangauer, M. J.; Viswanathan, V. S.; Ryan, M. J.; Bole, D.; Eaton, J. K.; Matov, A.; Galeas, J.; Dhruv, H. D.; Berens, M. E.; Schreiber, S. L.; McCormick, F.; McManus, M. T. Drug-Tolerant Persister Cancer Cells are Vulnerable to GPX4 Inhibition. *Nature* **2017**, *551*, 247–250.

(33) Liau, B. B.; Sievers, C.; Donohue, L. K.; Gillespie, S. M.; Flavahan, W. A.; Miller, T. E.; Venteicher, A. S.; Hebert, C. H.; Carey, C. D.; Rodig, S. J.; Shareef, S. J.; Najm, F. J.; Van Galen, P.; Wakimoto, H.; Cahill, D. P.; Rich, J. N.; Aster, J. C.; Suva, M. L.;

Patel, A. P.; Bernstein, B. E. Adaptive Chromatin Remodeling Drives Glioblastoma Stem Cell Plasticity and Drug Tolerance. *Cell Stem Cell* **2017**, *20*, 233–246.e237.

(34) Hassannia, B.; Vandenabeele, P.; Vanden Berghe, T. Targeting Ferroptosis to Iron Out Cancer. *Cancer Cell* **2019**, *35*, 830–849.

(35) Viswanathan, V. S.; Ryan, M. J.; Dhruv, H. D.; Gill, S.; Eichhoff, O. M.; Seashore-Ludlow, B.; Kaffenberger, S. D.; Eaton, J. K.; Shimada, K.; Aguirre, A. J.; Viswanathan, S. R.; Chattopadhyay, S.; Tamayo, P.; Yang, W. S.; Rees, M. G.; Chen, S.; Boskovic, Z. V.; Javaid, S.; Huang, C.; Wu, X.; Tseng, Y. Y.; Roider, E. M.; Gao, D.; Cleary, J. M.; Wolpin, B. M.; Mesirov, J. P.; Haber, D. A.; Engelman, J. A.; Boehm, J. S.; Kotz, J. D.; Hon, C. S.; Chen, Y.; Hahn, W. C.; Levesque, M. P.; Doench, J. G.; Berens, M. E.; Shamji, A. F.; Clemons, P. A.; Stockwell, B. R.; Schreiber, S. L. Dependency of a Therapy-Resistant State of Cancer Cells on a Lipid Peroxidase Pathway. *Nature* **2017**, *547*, 453–457.

(36) Oxnard, G. R. The Cellular Origins of Drug Resistance in Cancer. *Nat. Med.* **2016**, *22*, 232–234.

(37) Doll, S.; Proneth, B.; Tyurina, Y. Y.; Panzilius, E.; Kobayashi, S.; Ingold, I.; Irmler, M.; Beckers, J.; Aichler, M.; Walch, A.; Prokisch, H.; Trumbach, D.; Mao, G.; Qu, F.; Bayir, H.; Fullekrug, J.; Scheel, C. H.; Wurst, W.; Schick, J. A.; Kagan, V. E.; Angeli, J. P.; Conrad, M. ACSL4 Dictates Ferroptosis Sensitivity by Shaping Cellular Lipid Composition. *Nat. Chem. Biol.* **2017**, *13*, 91–98.

(38) Dixon, S. J.; Winter, G. E.; Musavi, L. S.; Lee, E. D.; Snijder, B.; Rebsamen, M.; Superti-Furga, G.; Stockwell, B. R. Human Haploid Cell Genetics Reveals Roles for Lipid Metabolism Genes in Nonapoptotic Cell Death. *ACS Chem. Biol.* **2015**, *10*, 1604–1609.

(39) Meng, H.; Liong, M.; Xia, T.; Li, Z.; Ji, Z.; Zink, J. I.; Nel, A. E. Engineered Design of Mesoporous Silica Nanoparticles to Deliver Doxorubicin and P-Glycoprotein siRNA to Overcome Drug Resistance in a Cancer Cell Line. *ACS Nano* **2010**, *4*, 4539–4550.

(40) Idelchik, M. D. P. S.; Begley, U.; Begley, T. J.; Melendez, J. A. Mitochondrial ROS Control of Cancer. *Semin. Cancer Biol.* **2017**, *47*, 57–66.

(41) Stockwell, B. R.; Angeli, J. P. F.; Bayir, H.; Bush, A. I.; Conrad, M.; Dixon, S. J.; Fulda, S.; Gascon, S.; Hatzios, S. K.; Kagan, V. E.; Noel, K.; Jiang, X.; Linkermann, A.;

Murphy, M. E.; Overholtzer, M.; Oyagi, A.; Pagnussat, G. C.; Park, J.; Ran, Q.; Rosenfeld, C. S.; Salnikow, K.; Tang, D.; Torti, F. M.; Torti, S. V.; Toyokuni, S.; Woerpel, K. A.; Zhang, D. D. Ferroptosis: A Regulated Cell Death Nexus Linking Metabolism, Redox Biology, and Disease. *Cell* **2017**, *171*, 273–285.

(42) Tsubouchi, K.; Araya, J.; Yoshida, M.; Sakamoto, T.; Koumura, T.; Minagawa, S.; Hara, H.; Hosaka, Y.; Ichikawa, A.; Saito, N.; Kadota, T.; Kurita, Y.; Kobayashi, K.; Ito, S.; Fujita, Y.; Utsumi, H.; Hashimoto, M.; Wakui, H.; Numata, T.; Kaneko, Y.; Mori, S.; Asano, H.; Matsudaira, H.; Ohtsuka, T.; Nakayama, K.; Nakanishi, Y.; Imai, H.; Kuwano, K. Involvement of GPx4-Regulated Lipid Peroxidation in Idiopathic Pulmonary Fibrosis Pathogenesis. *J. Immunol.* **2019**, *203*, 2076–2087.

(43) Zhang, Z.; Yao, Z.; Wang, L.; Ding, H.; Shao, J.; Chen, A.; Zhang, F.; Zheng, S. Activation of Ferritinophagy is Required for the RNA-Binding Protein ELAVL1/HuR to Regulate Ferroptosis in Hepatic Stellate Cells. *Autophagy* **2018**, *14*, 2083–2103.

(44) Stockwell, B. R.; Angeli, J. P. F.; Bayir, H.; Bush, A. I.; Conrad, M.; Dixon, S. J.; Fulda, S.; Gascón, S.; Hatzios, S. K.; Kagan, V. E.; Noel, K.; Jiang, X.; Linkermann, A.; Murphy, M. E.; Overholtzer, M.; Oyagi, A.; Pagnussat, G. C.; Park, J.; Ran, Q.;

Rosenfeld, C. S.; Salnikow, K.; Tang, D.; Torti, F. M.; Torti, S. V.; Toyokuni, S.; Woerpel, K. A.; Zhang, D. D. Ferroptosis: A Regulated Cell Death Nexus Linking Metabolism, Redox Biology, and Disease. *Cell* **2017**, *171*, 273-285.

(45) Gao, Z.; He, T.; Zhang, P.; Li, X.; Zhang, Y.; Lin, J.; Hao, J.; Huang, P.; Cui, J. Polypeptide-Based Theranostics with Tumor-Microenvironment-Activatable Cascade Reaction for Chemo-ferroptosis Combination Therapy. *ACS applied materials & interfaces* **2020,** *12*, 20271-20280.

# TABLE OF CONTENTS